TGRS-2024-02369

Mitigation of Decorrelation and Atmospheric Noise in InSAR Time-series, with Application to Postseismic Deformation following the 2021 Haiti Earthquake

S. Vajedian, *Missouri University of Science and Technology*, J. Maurer, *Missouri University of Science and Technology,* Z. Yin*, Scripps Institution of Oceanography, University of California San Diego,* J. Hasse, *Scripps Institution of Oceanography, University of California San Diego*

***Abstract*— Geodetic analysis of postseismic responses to major earthquakes offers insight into potential subsequent seismic activities and aseismic strain release. Interferometric Synthetic Aperture Radar (InSAR) provides a particularly high-resolution imaging capability for such transient events, particularly in regions without dense Global Navigation Satellite Systems (GNSS) networks. However, InSAR suffers from decorrelation errors and atmospheric noise, which can distort the interpretation of deformation patterns. To take a step towards addressing these challenges, this study introduces an advanced InSAR processing workflow and applies it to Sentinel-1 observations of postseismic deformation following the 2021 Haiti earthquake. We address decorrelation errors by employing phase linking through the Fine Resolution InSAR with Generalized Eigenvectors (FRInGE) method. We compare three methods for mitigating atmospheric effects, including a grouped Independent Component Analysis (ICA) method, and find that ICA performs best in removing atmosphere. Without applying these methods most of the signal is lost or hidden in the noise; after processing transient postseismic deformation, likely related to shallow fault creep, can be observed over ~3 months following the earthquake on the eastern EPGFZ. We compare the estimated cumulative slip to that obtained from ALOS-2 observations and find a good match, with ~3 cm of differential displacement on either side of the EPGFZ east of the rupture area. Our workflow provides a method for more precise characterization of localized transient deformation signals using C-band InSAR.**

***Index Terms*—InSAR, Atmospheric correction, Decorrelation, Postseismic, transient deformation, Phase linking, ICA**

I. INTRODUCTION

In the realm of geophysical research, Interferometric Synthetic Aperture Radar (InSAR) has been recognized for its precision in monitoring Earth's surface deformation. Its ability to detect mm- to cm-scale deformations over large areas provides unparalleled insights into tectonic activities. Yet, when applied to regions with mountainous landscapes and dense vegetation, InSAR encounters specific challenges. Tropospheric and ionospheric delays are larger and more variable at low latitudes and tropical areas, which significantly affect the accuracy of InSAR measurements (e.g., Hanssen, 2001; Bekaert et al., 2020; Zebker, 2021). Decorrelation is particularly problematic with Sentinel-1 C-band data, especially in non-arid regions.

Decorrelation of interferograms occurs when the scattering properties of a pixel changes between acquisitions. This occurs, for some examples, as a result of vegetation growth, snow cover in one image but not the other, or as a result of the ground breaking in a landslide or earthquake. In tropical locations like Haiti, decorrelation is very problematic with shorter wavelength sensors like Sentinel-1 (C-band, ~5 cm) due to a combination of factors including a lack of permanent infrastructure, rapid vegetation growth, and erosion during heavy rain events. As a result, C-band interferograms with a temporal baseline of more than a few weeks often completely decorrelate (Supp. Fig. S1). Bekaert et al. (2020), although not working in a tropical area, developed an InSAR-based method for mapping and monitoring slow-moving landslides in Nepal. They highlighted challenges posed by precipitation and vegetation that contributed to decorrelation noise in their study. Persistent scatterer (PS) pixel methods can be applied in cases where there are pixels containing strong, stable reflectors like buildings and bare rock (Ferretti et al., 2000, 2001; Colesanti et al., 2003; Hooper et al., 2004, 2007; Shanker and Zebker, 2007; Zebker et al., 2007), but in the case of Haiti, few stable pixels are available because of dense vegetation and little infrastructure. New methods have recently been developed that utilize statistical filtering of both PS pixels and distributed scatterer (DS) pixels in order to overcome decorrelation (e.g., Ferretti et al., 2011, Cao et al., 2016; Ansari et al., 2018; Even

This work was supported by the European Space Agency (ESA), the Japanese Aerospace Exploration Agency (JAXA), the National Science Foundation RAPID Grant (EAR-2150704), the NSF Office of Advanced Cyberinfrastructure program (OAC-1834807), the NASA FINESST program (80NSSC22K1533), the NSF EarthScope program (EAR-1147435, EAR-1424374, EAR-1614875), and NASA's Earth Surface and Interior Program (80NSSC22K0464). Additional support for S. Vajedian from a Missouri S&T block grant by the Taylor Geospatial Institute. (Corresponding author: H. Yin).

Dr. S. Vajedian is with the Geological Engineering department, Missouri University of Science and Technology, Rolla, MO, USA (e-mail: s.vajedian@mst.edu), Dr. J. Maurer is an assistant professor with the Geological Engineering department, Missouri University of Science and Technology, Rolla, MO, USA (email: jmaurer@mst.edu), H. Zoe. Yin is a PhD candidate in geophysics at Scripps Institution Oceanography at University of California San Diego (hyin@ucsd.edu). J. Hasse is a Professor in geophysics at Scripps Institution Oceanography at University of California San Diego (jhaase@ucsd.edu)

& Schulz, 2018). The Fine Resolution InSAR with Generalized Eigenvectors (FRInGE) algorithm is an open-source software package that provides PS+DS processing and has been shown to drastically reduce decorrelation and increase the number of useable data compared to normal time-series processing methods, even in highly vegetated areas (Dutta & Maurer, 2024). The key feature of FRInGE is its ability to leverage the interferometric covariance matrix for each DS and its surrounding neighborhood of statistically-similar pixels, as well as the phase history of each PS (Fattahi et al., 2019). By using a statistical phase estimation technique to identify and average similar pixels, FRInGE processing produces many more high-quality pixels than either PS or DS processing by themselves.

Numerous studies have looked at the best ways to reduce tropospheric noise (Hooper et al., 2012; Bekaert et al., 2015; Murray et al., 2019; Yu et al., 2017; Yu et al., 2018a; Yu et al., 2018b; Cao et al., 2021; Jolivet et al., 2011; Hooper et al., 2012; Bekaert et al., 2015b). Several software packages and online services, including the Raytracing Atmospheric Delay Estimator for Radar (RAiDER) package and the Generic Atmospheric Correction Online Service (GACOS) service, leverage globally available Numerical weather prediction (NWP) model outputs to produce tropospheric predictions. NWP models are available from the European Centre for Medium-Range Weather Forecasts (ECMWF), NASA's Global Modeling and Assimilation Office (GMAO), and NOAA's High-resolution rapid-refresh (HRRR) model. These NWP models can be used to compute predicted tropospheric delays to correct InSAR observations, but the performance of such models is usually not good enough to provide highly accurate displacement estimates for low-magnitude, transient deformation without additional correction methods (Bekaert et al., 2015; Maubant et al., 2020). Few studies have been done using InSAR in tropical areas for transient deformation, but one such study conducted by Maubant et al. (2020) used Independent Component Analysis to remove tropospheric noise in InSAR time series covering the 2017–2018 slow slip event in Guerrero, Mexico. The ICA method fits within a broader category of corrections that have been tested for use with InSAR using artificial intelligence (AI) (Anantrasirichai et al., 2018; Shamshiri et al., 2020; Rouet-Leduc et al., 2021). ICA worked well in that case to remove tropospheric noise, but two problems with that study were that most pixels in the deforming area were lost due to decorrelation, and there was no quantitative means of deciding which independent components were related to deformation, and which were related to troposphere. This ambiguity exists in all decomposition methods, and the only way to decide which subset of components to retain is to have an independent source of reliable displacements, such as a GNSS station, with which to compare. In Haiti we do not have such an independent source of information.

A. The 2021 Haiti Earthquake

The Enriquillo-Plaintain Garden fault zone (EPGFZ) is a major left-lateral strike-slip geological structure in southwestern Haiti. Historical records, corroborated by geologic data, reveal that the EPGFZ or nearby faults in the region have experienced large M_W7+ earthquakes in 1701, 1751, and 1770 (Mann et al., 2002; Prentice et al., 2010; Flores et al., 2011; Martin & Hough, 2022; Hough et al., 2023). More recently, the M_W7.0 2010 Leogane earthquake ruptured a blind thrust fault next to the EPGFZ (Calais et al., 2010, Hayes et al., 2010; DeRoches et al., 2011; Mercier de Lépinay et al., 2011; Symithe et al., 2013), and the M_W7.2 Tiburon Peninsula event ruptured the EPGFZ or a nearby fault in 2021 (Calais et al., 2022; Maurer et al., 2022; Okuwaki & Fan, 2022). These events highlight the need to better understand the tectonic dynamics in the region and quantify seismic hazard on the rest of the EPGFZ, in particular in the seismic gap left between the 2010 and 2021 earthquakes. This unruptured segment of the fault includes the western end of the Lake Miragoâne step-over and was characterized by a lack of aftershocks and fault creep (Douilly et al., 2013; Douilly et al., 2022; Yin et al., 2022; Fig. 1). These observations have spurred questions regarding the seismic hazard of the area and the tectonic processes responsible for the gap (e.g., Douilly et al., 2013; U.S. Geological Survey (2021); Martin & Hough, 2022).

B. Our approach

In this study, we investigate postseismic slip on the EPGFZ in the seismic gap between the 2010 and 2021 earthquake ruptures. We utilize InSAR observations from Sentinel-1 to develop displacement time-series, using FRInGE to address decorrelation and atmospheric corrections to address tropospheric noise and assess which tropospheric correction method performs best. We compare cumulative displacements derived from the Sentinel-1 time-series analysis with two ALOS-2 interferograms that cover the whole postseismic time period in order to assess the reliability of the results. The analysis confirms the occurrence of transient deformation on the EPGFZ in the seismic gap region in the ~3 month period following the 2021 earthquake, with displacements suggestive of shallow fault creep amounting to ~M_W5.3 magnitude equivalent.

II. Data and Methods

A. InSAR Data

Our analysis incorporated surface displacements derived from ascending track 004 and descending track 142 of Sentinel-1, as well as ascending track 042 of ALOS-2. The spatial footprint of these tracks can be seen in Fig. 1. ALOS-2 has a wavelength of approximately 22 cm, while Sentinel-1 is approximately 5.6 cm. The Sentinel-1 descending data span from 2021-08-15to 2022-01-30 (168 acquisitions total), and the ascending data from 2021-08-19 to 2022-02-01 (166 acquisitions total). We used 3 acquisitions available from ALOS-2 (2021-01-01, 2021-08-27, and 2021-12-31) in the high-resolution StripMap mode and all of these were in the ascending direction. We accessed Single-look complex (SLC) data for Sentinel-1 from the Alaska Satellite Facility. ALOS-2 data was provided from JAXA through an individual research grant.

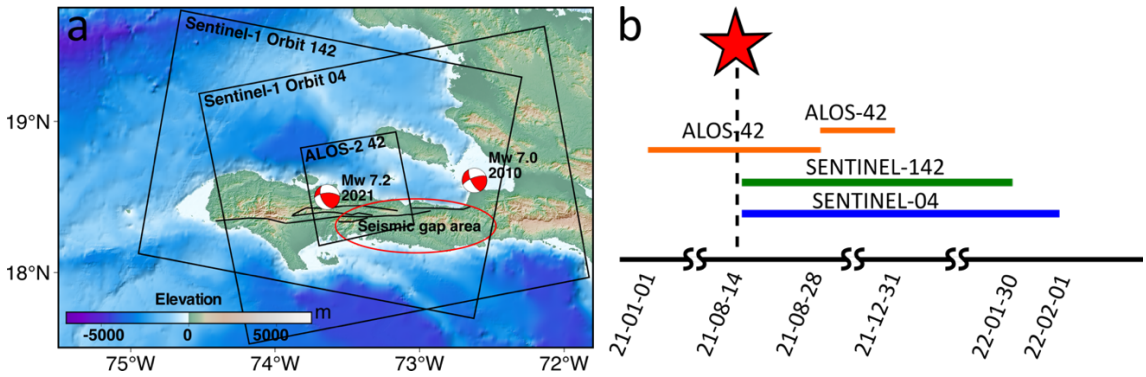

Fig. 1. Overview of satellite data used in this study. (a) Satellite frame footprints from Sentinel-1 and ALOS-2 are superimposed on a topographic map view. (b) Time span of each satellite track, color-coded by track: Orange for ALOS-2 data, green for descending Sentinel-1 tracks, and blue for ascending Sentinel-1 tracks. Note that the ALOS-2 bars represent the available interferograms, while the Sentinel-1 bars have many acquisitions available during the specified time periods.

B. ALOS-2 Processing

Number For the ALOS-2 dataset, processing is straightforward because there are only two interferograms and correlation is much better for the longer wavelength L-band data (~22 cm). The interferometric pair spanning from 2021-01-01 to 2021-08-27 encompasses the August 2021 earthquake and, as such, predominantly captures the coseismic deformation, which masks the postseismic signal. To remove the coseismic signal from the ALOS-2 interferograms, we utilized the coseismic slip distribution from Maurer et al., 2022, by projecting the modelled surface deformations into the Line of Sight (LOS) of the observing satellite (Supp. Fig. S2). We did not remove a plane from the displacements because of the possibility of removing some component of the coseismic and postseismic signals.

C. Sentinel-1 data processing

To detail the Sentinel-1 data processing corrections used in our study, we present a workflow diagram in Fig. 2. This flowchart shows how the processing workflow we developed to address the two primary challenges we faced: signal decorrelation and tropospheric noise. The overall workflow includes four major steps. Initially, standard stack processing is performed, which includes co-registration and removal of topographic phase, using ISCE2. We acquired SLC images in the Terrain Observations with Progressive Scans in azimuth (TOPS) mode, with initial stack processing done using the InSAR Scientific Computing Environment (ISCE) v.2 software, specifically the Sentinel-1 stack processor, "stackSentinel.py." Step 2 is to use FRInGE, an open-source InSAR processing technique developed by Fattahi et al. (2019) to process PS+DS pixels, which significantly reduced signal decorrelation. The algorithm uses an eigenvalue decomposition of the full interferometric matrix of pairs (i.e., all possible interferometric pairs) in order to reconstruct the phase history of each pixel (Mirzaee et al., 2023; Dutta & Maurer, 2024). FRInGE produces wrapped phase time-series, which are then unwrapped using snaphu (Chen & Zebker, 2001; Chen & Zebker, 2002). Using traditional SBAS techniques in southern Haiti result in significant loss of coherence for temporal baselines >24 days, while the FRInGE method has been successfully applied in studies of highly vegetated areas and works well to retain many pixels (Samiei-Esfahany et al., 2016; Ansari et al., 2017). By applying phase linking through the FRInGE software, we are able to retain nearly all pixels in southern Haiti and mitigate the impact of decorrelation on our analysis. We use a reference pixel located on the fault trace to de-reference the time-series stack.

Step 3 of the process is to remove tropospheric noise as much as possible. To do this, we tested three methods: 1) atmospheric phase screen (APS) estimation via common date stacking (Tymofyeyeva & Fialko, 2015), 2) APS estimation from NWP models using the RAiDER package (see Data and Resources), and 3) using Independent Component Analysis (ICA) to isolate the deformation component of the time-series (Ebmeier, 2016; Gaddes et al., 2018; Maubant et al., 2020; Gualandi & Liu, 2021). Each of the methods is described in more detail in Section 2.3.2. The last step in our workflow is to calculate the cumulative displacement from the time series, which we do by fitting a logarithmic function to the time-series:

$$\log(t) = a\log(1 + (t - tq)/\tau) + b \quad (1)$$

where t represents the time of observation, tq is the time of the earthquake, and a, b, and τ are the model parameters to be determined. τ in particular is the decay time constant.

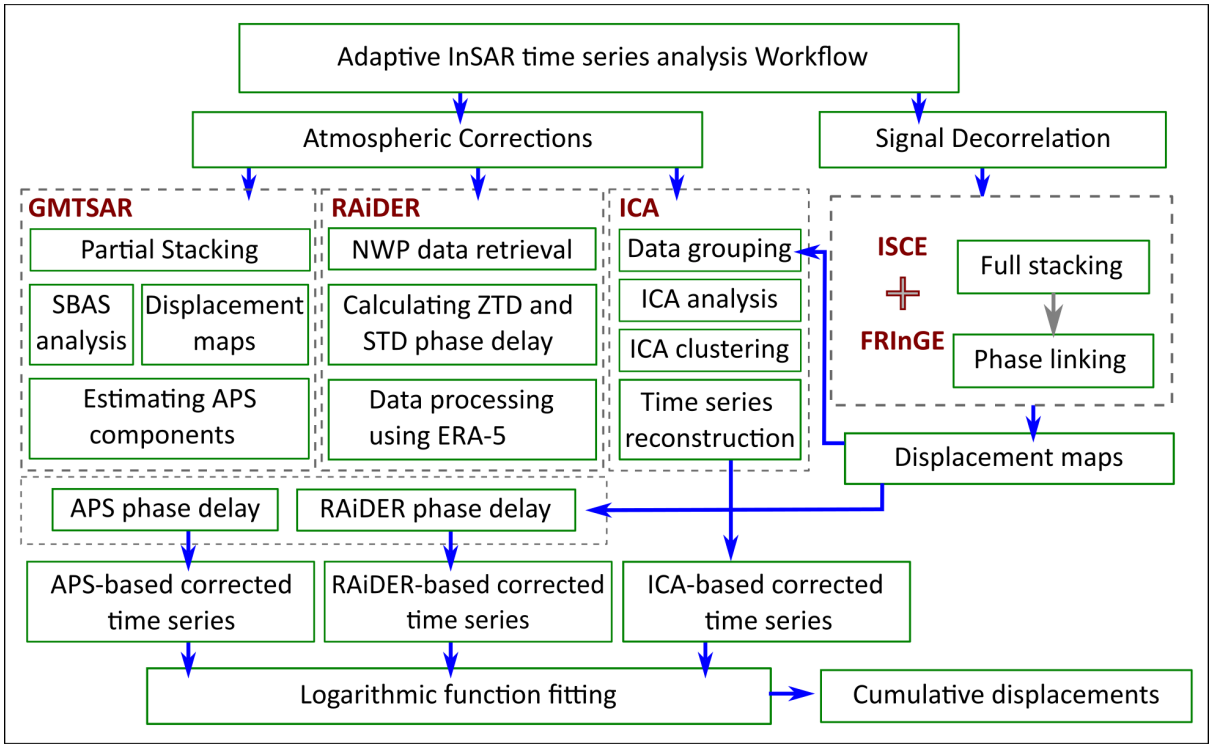

Fig. 2. Workflow diagram detailing the Sentinel-1 data processing workflow employed in this study. The flowchart addresses two primary challenges: signal decorrelation, mitigated through phase linking using the FRInGE package, and atmospheric phase delay, tackled using three distinct methods: statistical-based correction (GMTSAR), RAiDER correction, and ICA analysis.

D. Tropospheric Phase Delay Corrections

Unlike the decorrelation problem, there is no standard or community-accepted single way of correcting for the troposphere. Tropospheric delays are often categorized into two separate processes, a "stratified" component, which is correlated with topography and generally long-wavelength, and a "turbulent" component, which is caused by small-scale variations in water vapor, temperature, and pressure. The turbulent component is particularly challenging to model and correct. As noted above, methods for correcting the troposphere generally fall into three classes, 1) those using auxiliary data, particularly global NWP models (e.g., Webley et al., 2002; Jolivet et al., 2014; Bekaert et al., 2015b; Cao et al., 2021), 2) those using statistical filtering or averaging techniques (Tymofyeyeva & Fialko, 2015; Kirui et al., 2022), and 3) decomposition methods that attempt to identify and extract deformation signals from the time-series (e.g., Maubant et al., 2020; Gualandi & Liu, 2021). We test methods representing each of these classes of algorithms.

E. Correction based on NWP

NWP models such as the ECMWF-ERA5 model provide global weather model products that include predictions for pressure, temperature, and water vapor, from which propagation delays can be analytically computed. The products generated by NWP models represent best estimates of the state of the atmosphere at a particular date, time, and location (Kalnay et al., 1996). Although NWP models have improved significantly in the last decades due to increased observations and improved computational resources, model physics, and assimilation capabilities, their accuracy is still limited by low resolution model grids, incomplete model physics, and other factors (e.g., Hong & Dudhia, 2012). NWP models have been applied to calculate tropospheric delays for InSAR in many studies (e.g., Hooper et al., 2012; Jolivet et al., 2014; Bekaert et al., 2015; Cao et al., 2021). We use the ECMWF-ERA5 model to calculate delays as it is globally and freely available, and has a higher resolution that the GMAO model. We use the open-source RAiDER package (see Data and Resources) to download ERA-5 model predictions of pressure, temperature, and water vapor and calculate tropospheric delays at the location of the InSAR pixels, which are then directly dereferenced and subtracted from the displacement time-series.

F. Statistical filtering using common-date stacking

The statistical atmospheric correction method implemented in GMTSAR capitalizes on the redundancy present in multi-temporal InSAR datasets (Tymofyeyeva & Fialko, 2015). The method assumes that tropospheric delays are uncorrelated in time in order to remove the atmospheric contribution to the displacement time-series. The method relies solely on the interferograms themselves and does not require external data, which ensures global applicability and helps with reliability, but does require a highly redundant network of interferograms. The method takes differences of pairs of interferograms having a common date, in order to cancel out the deformation component on that date. By averaging a large number of pairs having the

same common date, the atmospheric phase screen for that date is estimated. The process is repeated for each date, and the time-series of atmospheric noise is removed from the InSAR time-series (Supp. Fig.'s S3-S6).

G. ICA-based correction

ICA is a computational technique designed to separate multivariate signals into additive, independent components. It decomposes mixed signals into components that are mutually independent and exhibit non-Gaussian distributions (Hyvärinen and Oja, 1997). Given a set of source signals, s(t), and their corresponding observations, x(t), the mixing process can be represented as:

$$x(t) = As(t) \quad (2)$$

where **A** is an unknown mixing matrix. If **A** is square, the independent components, *s*, can be estimated using its inverse, W:

$$s(t) = Wx(t) \quad (3)$$

Before ICA application, observations are standardized to intermediate variables with zero mean and unit variance. Whitening is achieved using the Eigenvalue Decomposition (EVD) of the covariance matrix of $x(t)$, transforming $x(t)$ to have uncorrelated components with equal variances:

$$x_\omega = VD^{-1/2}V^T x \quad (4)$$

Here, V contains eigenvectors, and D has eigenvalues. Whitening simplifies the ICA process by reducing the number of unknown parameters, converting the mixing matrix A into an orthogonal form.

As noted in the Introduction, ICA-based methods have been used to estimate and remove tropospheric and other noise sources from InSAR data, but suffers from an ambiguity as to which components should be labeled as deformation versus tropospheric noise unless the form of the deformation signal is known. Typically, practitioners try to identify the desired source(s) by visual inspection of which independent components match the known deformation signal. Automatic selection of sources is important to develop because the true deformation signal may be unknown (as in the case of the 2021 Haiti earthquake, where no continuous GNSS stations were operating). To address this challenge, we introduce a quantitative method to determine which ICA components are related to deformation signals, inspired by a method proposed by Ebmeier (2016) and drawing on principles laid out by Hyvärinen and Ramkumar (2013). It is based on the following steps and illustrated in Fig. 3:

1. Unwrapped interferograms are split into two groups by dates, so that the dates sampled by one group are not a part of the second group, but both groups contain the full range of dates. Both groups must sample the deformation process in a similar manner, so we use every other date to split the interferograms. I.e., interferograms from one group contain only the 1st date from the time-series sequence, 3rd date, 5th date, and so on, while interferograms from the second ground only sample the 2nd date, 4th date, etc.
2. Two sets of independent components (ICs) are constructed by performing ICA analysis separately on each group of interferograms. Choice of the number of independent components is determined by the total number of dates in each group's time series sequence, ensuring that a full set of ICs is extracted for each group to accurately represent the observed deformation dynamics.
3. ICs are compared across the two groups. Assuming again that tropospheric signals are uncorrelated in time (at least at time scales longer than the time period between every other acquisition), ICs that match between the two groups are identified as likely containing deformation signals. We use the *isctest* algorithm (Hyvärinen, 2011; Hyvärinen & Ramkumar, 2013) to compare and cluster ICs based on their similarity.
4. The interferograms in each group are reconstructed based on the ICs identified as corresponding to deformation signals.
5. Finally, we apply standard small-baseline subset (SBAS) processing to create the final time-series from the reconstructed interferograms.

An important limitation of the ICA method is that in practice it did not perform well with multiple deformation sources. Following the 2021 Haiti earthquake, postseismic deformation occurs both east and west of the main rupture (see Results below), but the mode of deformation is predominately uplift west of the hypocenter, compared to fault creep east of the hypocenter that is the focus of this study. ICA on the entire region did not perform well, possibly because more deformation sources would require splitting the data into more groups or independent components, which would require more observations to constrain the sources. Because we only have acquisitions every 12 days and the deformation only lasts ~3-4 months, we likely do not have enough samples to further divide the observations and still adequately resolve the separate sources. In order to isolate displacements due to fault creep east of the hypocenter, we apply the ICA method only to a limited region around that area.

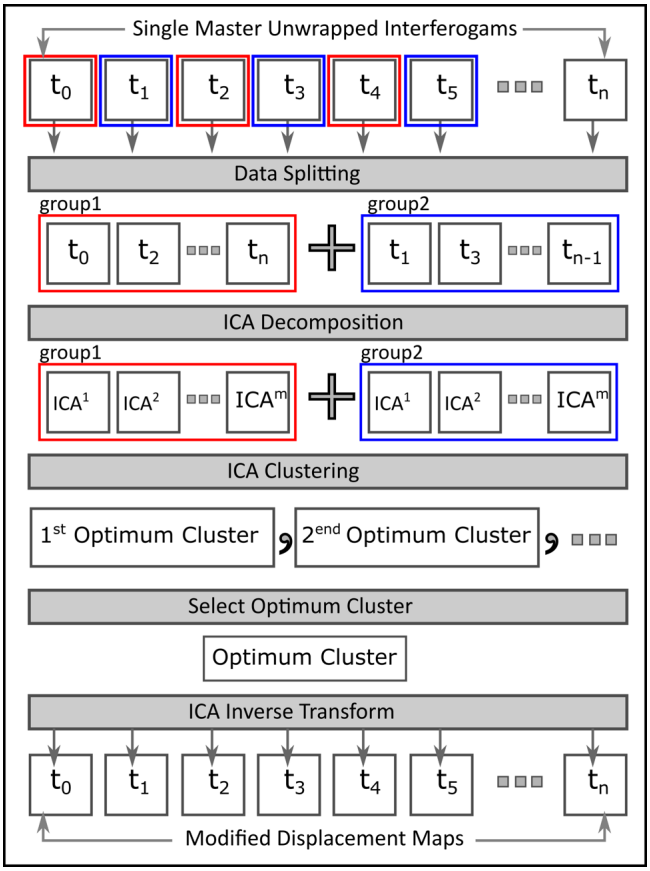

Fig. 3. Workflow diagram illustrating the processing steps involved in the ICA analysis for tropospheric correction.

III. Results for 2021 Haiti earthquake postseismic

A. Time-series comparison and cumulative displacements

To compare results from the different methods for tropospheric correction, Fig.'s 4-5 show cumulative displacements for the ascending and descending tracks before and after correction. The top row presents the output from FRInGE without any tropospheric adjustments, while the 2nd-4th rows illustrate the effects of each correction method individually. The left panel shows the performance for the full track width, while the right panel shows our study area. From a temporal perspective, Fig.'s 4g and 5g show time series plots at point P1 for the original data as well as after correction by each of the methods.

Comparing plots, the ICA does the best of all the correction methods at reducing the total noise in the images. Although some residual atmospheric noise is clearly still present, Supp. Table S1 shows that the ICA method applied to the ascending track results in cumulative displacements with an RMS reduction of 23%, compared to a 16% reduction using common-date stacking and 2% reduction using ERA-5. For the descending track, all methods perform better but ICA performed the best, reducing the RMS phase by 57%, compared to 48% with common date stacking and 20% with ERA-5.

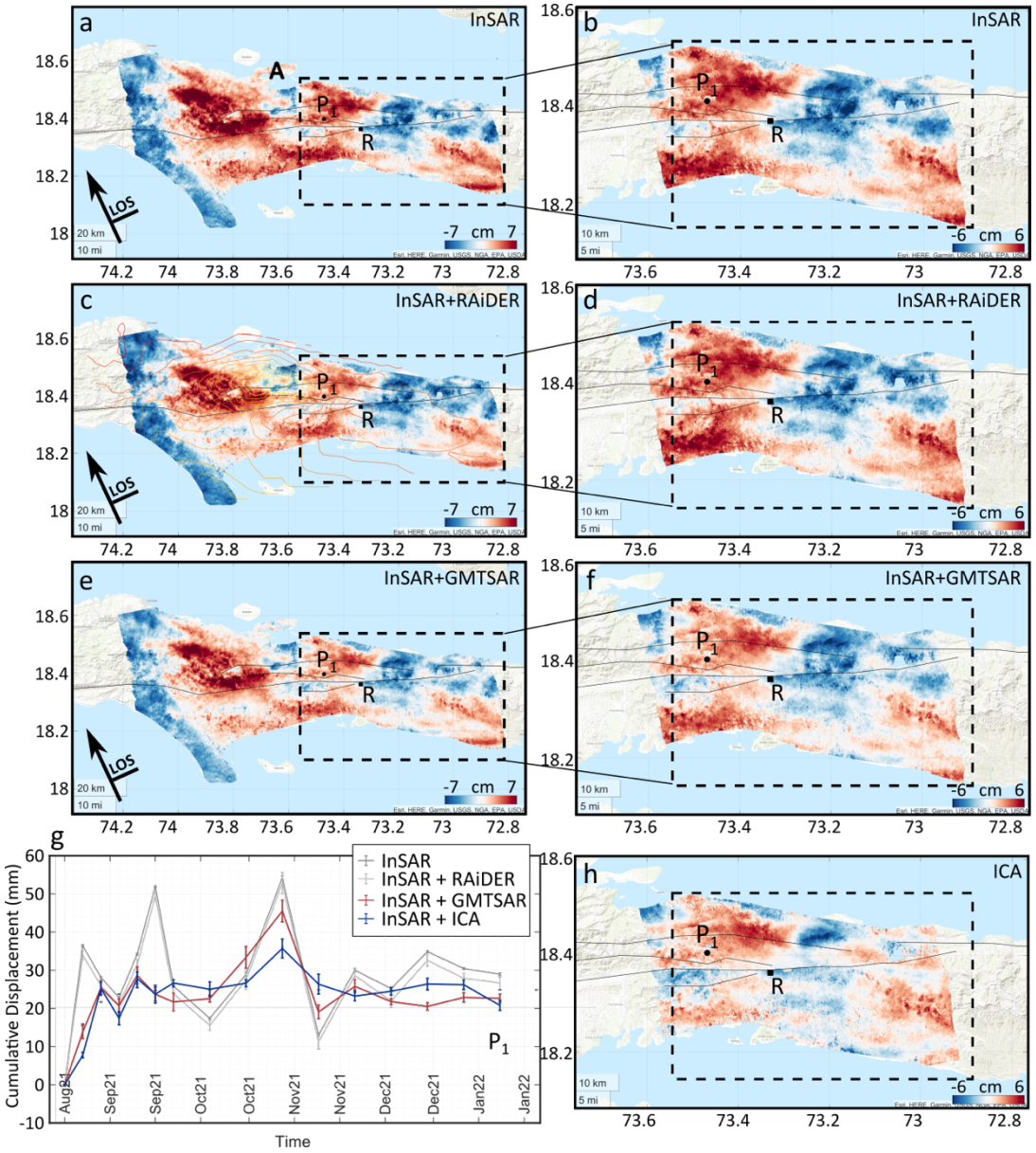

Fig. 4. Comparison of cumulative displacement from different tropospheric correction methods for ascending track. (a-b) Cumulative displacement derived from FRiNGE without any tropospheric correction (labeled as "InSAR"). (c-d) Displacement after applying ERA-5 correction (labeled as "InSAR + RAiDER"). (e-f) Cumulative displacement after correction with common date stacking. (g) Time series plots comparing the original data with the corrected at point P1 and the logarithmic fit. (h) Cumulative displacements for the reduced study area after correction using ICA. Point R, marking the reference point, is indicated in panels a, b, c, d, e, f, and h.

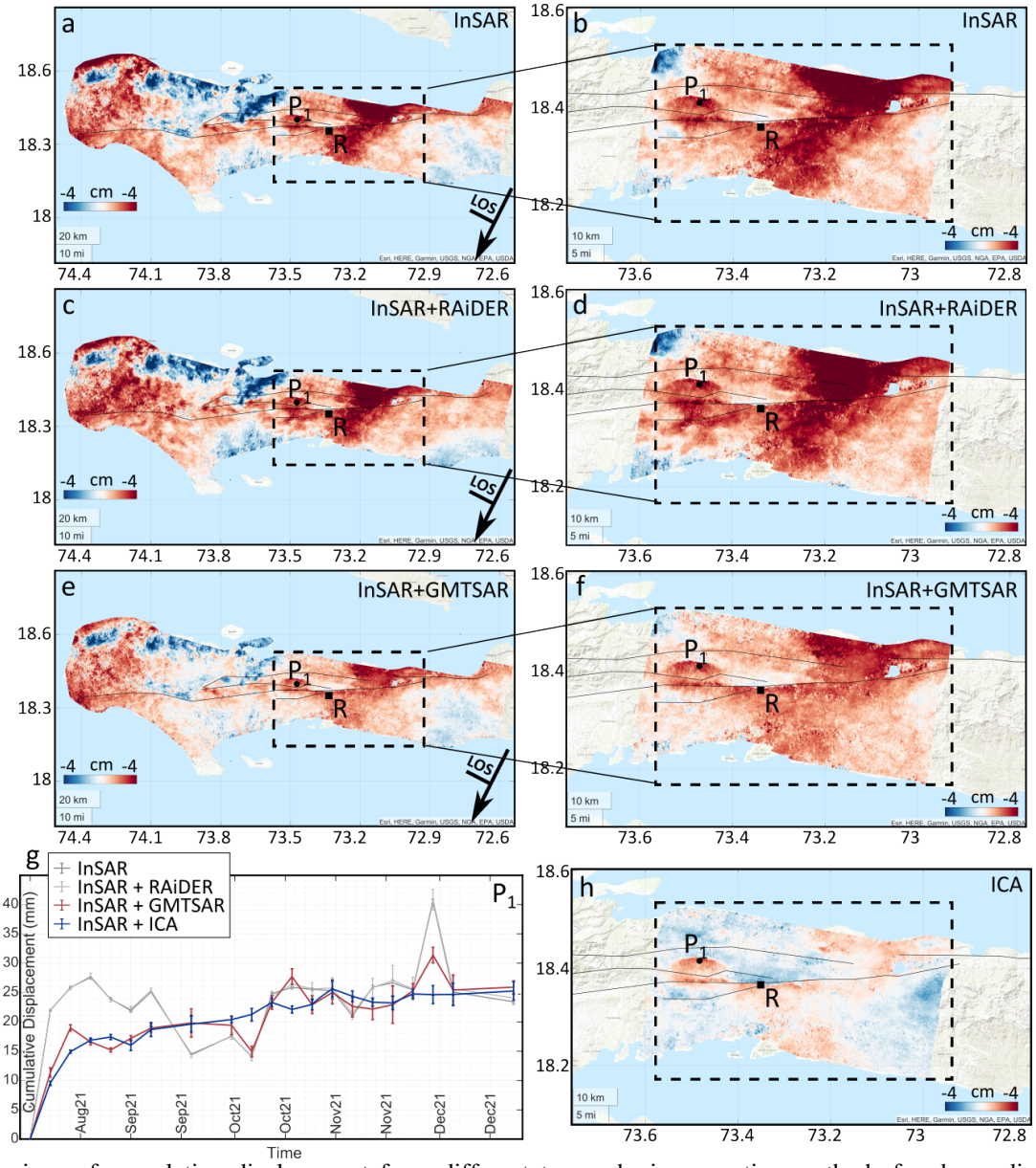

Fig. 5. Comparison of cumulative displacement from different tropospheric correction methods for descending track. (a-b) Cumulative displacement derived from FRiNGE without any tropospheric correction (labeled as "InSAR"). (c-d) Displacement after applying ERA-5 correction (labeled as "InSAR + RAiDER"). (e-f) Cumulative displacement after correction with common date stacking. (g) Time series plots comparing the original data with the corrected at point P1 and the logarithmic fit. (h) Cumulative displacements for the reduced study area after correction using ICA. Point R, marking the reference point, is indicated in panels a, b, c, d, e, f, and h.

Frictional afterslip should manifest as logarithmic time-dependent deformation, so we fit logarithmic functions to each pixel in the cumulative deformation maps shown in Fig.'s 4h and 5h using Eq. 1 (Fig. 6, Supp. Fig. S7). The results are similar to the cumulative offset maps in that the descending track is shows lower residual atmospheric noise and a clearer signal of the creep, including what appears to be several cases of small-scale faulting away from the EPGFZ, similar to what Yin et al. (2022) found. Faults from Maurer et al. (2022) are shown for reference in black. Displacements along the eastern EPGFZ are consistent with shallow left-lateral creep, although the ascending observations are noisy, with relative displacements across the fault on the order of ~3 cm.

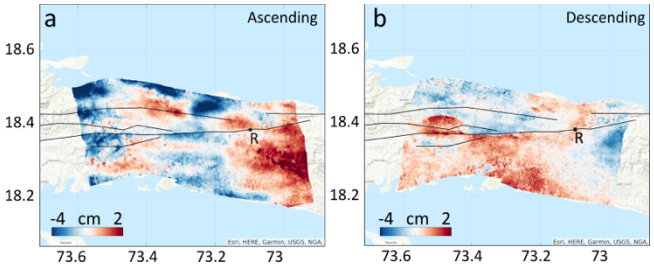

Fig. 6. Cumulative displacements obtained by fitting logarithmic functions to each pixel of the of the InSAR time-series. Faults from Maurer et al. (2022) are shown for reference

in black. (a) Ascending track displacements. (b) Descending track displacements.

B. Comparison with ALOS-2 Cumulative Displacements

We compare cumulative displacements estimated with ALOS-2 observations to those derived from fitting Sentinel-1 time-series. ALOS-2 is L-band data and has much better coherence than the Sentinel-1 observations, but does not provide good temporal sampling of the deformation.

Fig. 7a-c shows the ALOS-2 observations, and 7d shows profiles of cumulative displacement from ALOS-2 and the different troposphere correction methods. Fig. 7a shows the first interferogram corrected for the coseismic displacement and Fig. 7b shows the second covering the postseismic period from 2021-08-27 to 2021-12-31. Note that some large residual displacements are visible in Fig. 7a. Maurer et al. (2022) did not use this interferogram in their slip inversion, suggesting that their modeled coseismic slip did not fully capture the distribution of fault slip in this region. Fig. 7c shows the total postseismic displacements, summing both interferometric pairs with the estimated coseismic removed. Fig. 7d shows profiles of cumulative displacement derived from the ALOS-2 observations (black line) along the profile shown in Fig. 7c, as well as the corresponding Sentinel-1 observations (colored lines) with different corrections applied. The uncorrected, ERA-5 corrected, and common-date stacking-corrected profiles all show large deviations from the ALOS-2 observations that are not consistent with the expected left-lateral strike-slip motion of fault creep; while the ICA-corrected profile aligns fairly well with that from ALOS-2 (deviations of roughly ~1 cm), and is more consistent with left-lateral slip on the fault. ALOS-2 interferograms will still be affected by the troposphere and ionosphere, so the ALOS-2 displacements do not perfectly represent the deformation, but the long interferometric time-period provides a much higher signal-to-noise ratio per interferogram than Sentinel-1. In addition, note that the geometry from the ALOS-2 track is not exactly the same as for Sentinel-1, but is close enough to warrant a basic visual comparison.

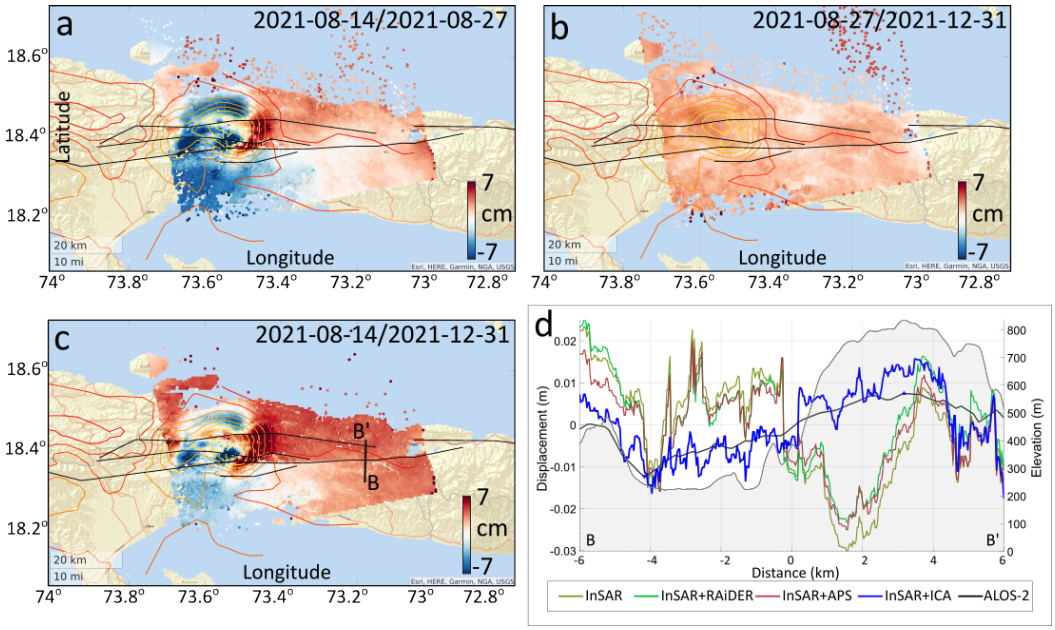

Fig. 7. (a-c) Interferometric pairs derived from ALOS-2 data. (a) Differenced map showing the LOS displacements between 2021-01-01 and 2021-08-27, after removing the modeled coseismic deformation based on the study by Maurer et al., 2022 (approximating displacements between 2021-08-14 and 2021-08-27). The original coseismic interferogram is shown in the Supplemental Material. (b) Postseismic LOS displacements between 2021-08-27 and 2021-12-31. (c) Total deformation, representing the sum of the two pairs (in panels a and b), spanning the combined post-earthquake period (2021-08-14 - 2021-12-31) for comparison with the Sentinel-1 A/B dataset. (d) Comparative profiles of cumulative LOS displacement vs. distance perpendicular to the EPGFZ fault line. The profiles represent displacements derived from standard InSAR processing (olive green), with RAiDER correction (bright green), additionally corrected with APS component reduction (red), and additionally corrected with ICA-based correction (blue). The reference profile from ALOS-2 observations is also depicted for benchmarking purposes (black). Topography is shown in shaded.

Fig. 8 provides a further comparison between ALOS-2 and the Sentinel-1 time-series cumulative displacements. The left-hand series of panels shows the same study area as above, while the right-hand series of panels zooms into the seismic gap region of the EPGFZ east of the 2021 earthquake hypocenter, in order to better show the results in the region with shallow fault creep. Fault creep is estimated by differencing displacements on either side of the fault and plotted as colored dots along the fault trace.

Fig. 8 shows surface displacements and fault creep estimates from ALOS-2 (Fig. 8a-b), Sentinel-1 time-series without any tropospheric corrections (Fig. 8c-d), and with the ICA correction (Fig. 8e-f). Fig. 8g shows the fault creep estimates as profiles along strike of the fault. The comparison is hindered by the residual coseismic deformation in the ALOS-2 interferograms, but it is clear that correction with the ICA method improves the match between Sentinel-1 and ALOS-2 results and shows more realistic fault creep patterns.

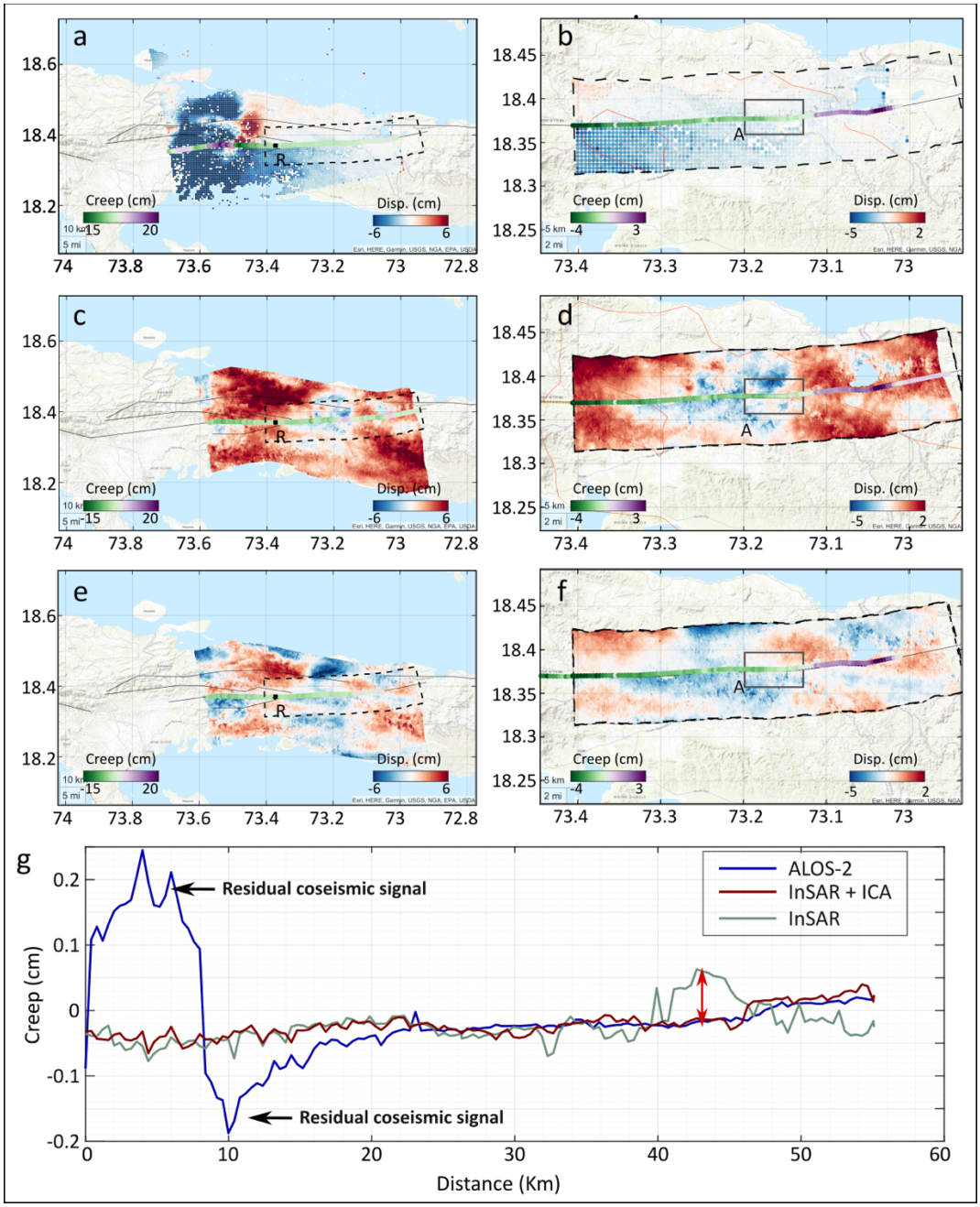

Fig. 8. Comparison of cumulative displacements from ALOS-2 and Sentinel-1, ascending data. (a), (c), and (e) show displacements for the whole study area, while (b), (d), and (e) focus on a smaller area around the EPGFZ east of the 2021 earthquake hypocenter. (a-b) Cumulative displacement from ALOS-2 with estimated coseismic displacements removed. Estimated cumulative fault creep is shown as colored dots along the EPGFZ fault line. (c-d) Equivalent views as in (a-b) but using the Sentinel-1 cumulative displacements without any corrections. (e-f) Equivalent views as in (a-b) using Sentinel-1 time-series with ICA correction. (g) Estimated cumulative fault creep along the entire line. Point R, indicated in the panels a,c and e, shows the location of the reference point.

For the descending track, we do not have ALOS-2 observations in stripmap mode as we do for ascending, so we show qualitatively the improvement in the estimated cumulative fault creep from ICA correction in Fig. 9. Similar to the ascending track, we see that the ICA-corrected results show much lower small-scale variability in the fault creep estimates, and much lower noise overall. Fault creep is clearly seen east of the hypocenter area. An area near the hypocenter, located at approximately 18.4N, 73.5W, shows up in the descending data that is likely an area of small-scale thrust faulting during or shortly after the earthquake, similar to the small-scale strike-slip faulting discussed in Yin et al. (2022).

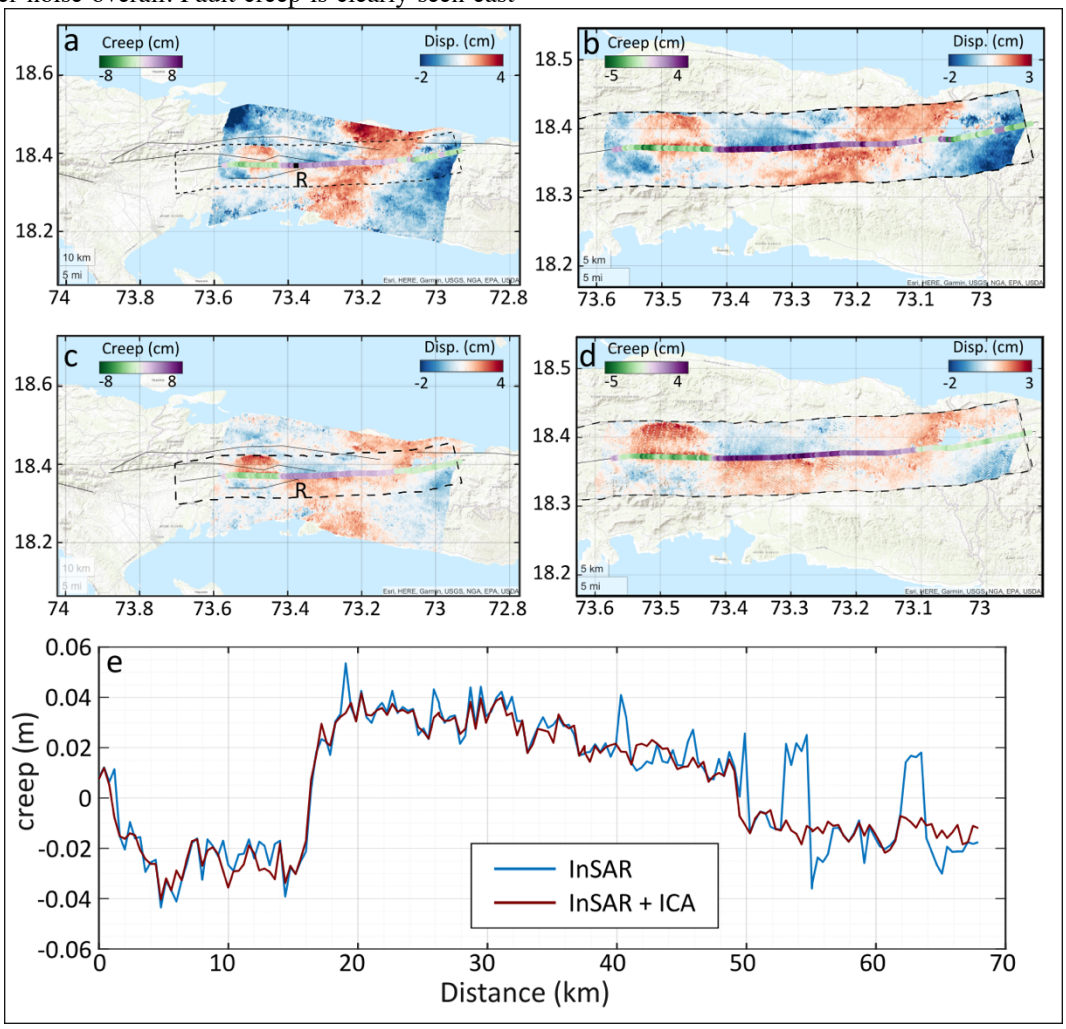

Fig. 9. Cumulative displacements and estimated fault creep from Sentinel-1, descending track, based on (a-b) the uncorrected time-series and (c-d) the ICA-corrected time-series. (e) Profile of estimated cumulative fault creep before and after ICA correction. Point R, indicated in the panels a,b,c,d, shows the location of the reference point.

IV. Discussion

A. When does the ICA method work well and when does it not?

In this study we have compared three methods for removing tropospheric noise from Sentinel-1 time-series: NWP model-based predictions of propagation delays, common-date stacking, and ICA decomposition of groups of interferograms. NWP models are currently insufficient in modeling the turbulent component of atmospheric propagation delays, and our study area represents an extreme case of turbulent atmosphere: highly mountainous topography coupled with high water vapor content and a very active weather system. In fact, Tropical Depression Grace struck Haiti on August 16th, only two days after the earthquake, during which time some of the early Sentinel-1 acquisitions were made. NWP models, while valuable for capturing broader atmospheric trends and the stratified component of the tropospheric noise, usually fail to capture the details of localized atmospheric disturbances (Siddique et al., 2019; Hu et al., 2018; Liu et al., 2015; Kumar et al., 2016). In comparison, the common-date stacking and ICA methods we tested utilize redundant interferograms to determine the atmospheric delays for each date without requiring auxiliary data. The common-date stacking method assumes that deformation signals are strictly linear (Tymofyeyeva & Fialko, 2015), while ICA requires a single type of deformation source, at least in practice for the number

of acquisitions we had. No one method seems to perform well under all circumstances, but the ICA method out-performed the others for our case with a single deformation source and highly turbulent atmospheric conditions.

While the ICA has proven capable of isolating the postseismic deformation signal from atmospheric noise, some residual troposphere remains even after correction by ICA and estimating cumulative deformation using logarithmic fitting. Further work is still needed to improve on the method, in particular whether and which combinations of correction methods could be used together to take advantage of the strengths of each. Application of artificial intelligence (AI) approaches have also been used for various aspects of the problem (e.g., Anantrasirichai et al., 2018; Shamshiri et al., 2020; Rouet-Leduc et al., 2021), but not much work has been done to use AI to remove troposphere from time-series; most work to date focuses on extracting a known deformation signal from noisy time-series. While beneficial for particular classes of deformation (e.g., volcanic deformation), such a template-matching style of method will be limited for identifying more general spatially-varying transient deformation that does not necessarily break the surface.

B. Afterslip on the EPGFZ

In this study, we find evidence for shallow fault creep on the EPGFZ east of the 2021 earthquake hypocenter. The displacements are consistent with left-lateral strike-slip motion, as evidenced by the opposite signs of deformation in the ascending and descending tracks. Analysis of the temporal evolution of afterslip east of the rupture in the gap area shows that it was consistent with logarithmic decay, indicative of frictional afterslip processes. These processes are typically governed by the redistribution of stress in the shallow crust following a seismic event (e.g., Diao et al., 2021; Fukuda & Johnson, 2021; Hong & Liu, 2021; Copley, 2014; Lange et al., 2014) We find ~2-3 cm of fault creep (line-of-sight) occurred over ~3 months following the earthquake, with most of the deformation happening in the first two weeks after the event (Fig.'s 4g, 5g). The limited spatial extent of the signal suggests that the creep was shallow. The displacements suggest a slipping patch <5 km deep and ~2-3 cm in magnitude over 30-40 km the fault, corresponding to a moment of $\sim 10^{17}$ N m, assuming a 30 GPa shear modulus, or ~M_W5.3 equivalent.

C. Other deformation following the 2021 Haiti earthquake

Although not the focus of our study, our results do have implications for deformation processes occurring elsewhere in the Tiburon Peninsula following the 2021 Haiti earthquake. When performing the analysis in this study, we processed data for the full Tiburon peninsula region, including areas both west and east of the 2021 earthquake. ICA analysis did not perform well with multiple deformation sources, as noted in the Methods section, but the time-series corrected using the common-date stacking and ERA-5 NWP model corrections both show evidence for postseismic displacements west of the hypocenter area following the earthquake, including some areas that appear to have experienced uplift. Deformation during the earthquake occurred on multiple faults, with evidence of very early postseismic deformation happening off the main EPGFZ fault trace (Maurer et al., 2022), so continued off-fault deformation is not entirely unexpected, but further analysis of those areas is needed to confirm the results shown in this study. Additionally, Yin et al. (2022) document multiple cases of small-scale strike-slip faulting throughout the Tiburon Peninsula, and some of the areas shown in their study also can be seen in our results (e.g., event "g" in their Fig. 7a). It is currently not known whether and how off-fault deformation accommodates some component of overall plate motion; studies in the western US and New Zealand have found that off-fault deformation may account for a third to a half of the total (e.g., Pollitz et al., 2022; Johnson et al., 2024). Thus, these small-scale faulting processes may add up to a non-negligible portion of the plate rate over time.

V. Conclusions

In this study, we have presented an advanced InSAR processing workflow using phase linking and ICA for tropospheric corrections, and applied the workflow to investigate postseismic displacements along the EPGFZ east of the 2021 Haiti earthquake, in a seismic gap between the 2010 and 2021 Haiti earthquakes. The methodology drastically improved coherence and reduced RMS variation in the estimated cumulative InSAR displacements from 1.7 to 0.75 cm for the descending track, an improvement of 57%, and from 2.09 cm to 1.6 cm for the ascending track, an improvement of 23%. We fit logarithmic functions to the resulting InSAR time-series and find peak cumulative differential displacements (creep) on the segment of the EPGFZ between the 2021 earthquake epicenter and Lake Miragone of ~3 cm in the line-of-sight. Cumulative creep estimates from Sentinel-1 derived with this methodology match those from ALOS-2. The displacements suggest shallow creep on the EGPFZ in the seismic gap region, with a total (aseismic) moment corresponding to a ~M_W5.3 earthquake. Further work is needed analyze the gap between the 2010 and 2021 Haiti earthquakes for seismic hazard. Our proposed methodology has proven successful in allowing us to utilize C-band time-series data in an area that normally would be very challenging due to decorrelation and atmospheric noise, paving the way for future work on transient deformation in this and similar areas around the world.

Data and Resources

For this study, we utilized a combination of open-source packages and freely available Sentinel-1 data provided by the European Space Agency (ESA) and ALOS2 data available through the Japan Aerospace Exploration Agency (JAXA). Interferograms were produced using GMTSAR (https://topex.ucsd.edu/gmtsar/) and ISCE

(https://github.com/isce-framework/isce2) packages, which are widely recognized tools in the InSAR processing community. The phase linking process was conducted using the FRInGE package (https://github.com/isce-framework/fringe), a robust tool for handling InSAR data.

Tropospheric correction based on global Numerical Weather Prediction (NWP) models was performed using the RAiDER package (https://github.com/dbekaert/RAiDER).

ACKNOWLEDGMENT

The authors thank the European Space Agency (ESA) for the rapid acquisition and distribution of Sentinel-1 data. The authors thank the Japanese Aerospace Exploration Agency (JAXA) for access to Advanced Land Observation Satellite (ALOS)-2 data which was made available under an individual proposal. Rapid ALOS-2 InSAR data processing was supported by a National Science Foundation RAPID Grant (Number EAR-2150704). H. Yin was supported by the NSF Office of Advanced Cyberinfrastructure program (Grant Number OAC-1834807) and the NASA FINESST program (Grant Number 80NSSC22K1533). The development of the GMTSAR software was supported by the National Science Foundation (NSF) through the NSF Office of Advanced Cyberinfrastructure program (Grant Number OAC-1834807), and the NSF EarthScope program (Grant Numbers EAR-1147435, EAR- 1424374, and EAR-1614875). J. Maurer and S. Vajedian carried out part of this work with funding from NASA's Earth Surface and Interior Program, (Grant Number 80NSSC22K0464). S. Vajedian was also supported in part by a block grant to Missouri S&T from the Taylor Geospatial Institute.

REFERENCES

[1] Anantrasirichai, N., Biggs, J., Albino, F., Hill, P., & Bull, D. (2018). Application of Machine Learning to Classification of Volcanic Deformation in Routinely Generated InSAR Data. Journal of Geophysical Research: Solid Earth, 123(8), 6592–6606. https://doi.org/https://doi.org/10.1029/2018JB015911

[2] Ansari, H., De Zan, F., & Bamler, R. (2018). Efficient Phase Estimation for Interferogram Stacks. IEEE Transactions on Geoscience and Remote Sensing, 56(7), 4109–4125. https://doi.org/10.1109/TGRS.2018.2826045

[3] Bekaert, D. P. S., Hooper, A., & Wright, T. J. (2015a). Reassessing the 2006 Guerrero slow-slip event, Mexico: Implications for large earthquakes in the Guerrero Gap. Journal of Geophysical Research: Solid Earth, 120(2), 1357–1375. https://doi.org/10.1002/2014JB011557

[4] Bekaert, D. P. S., Walters, R. J., Wright, T. J., Hooper, A. J., & Parker, D. J. (2015b). Statistical comparison of InSAR tropospheric correction techniques. Remote Sensing of Environment, 170, 40–47. https://doi.org/10.1016/j.rse.2015.08.035

[5] Bekaert, D. P. S., Handwerger, A. L., Agram, P., & Kirschbaum, D. B. (2020). InSAR-based detection method for mapping and monitoring slow-moving landslides in remote regions with steep and mountainous terrain: An application to Nepal. Remote Sensing of Environment, 249, 111983. https://doi.org/10.1016/j.rse.2020.111983

[6] Bevis, M., Businger, S., Herring, T.A., Rocken, C., Anthes, R.A., Ware, R.H. (1992) GPS meteorology: Remote sensing of atmospheric water vapor using the global positioning system. J. Geophys. Res, 97(15), pp.787-15. https://doi.org/10.1029/92JD01517

[7] Çakır, Z., Ergintav, S., Ozener, H., Doğan, U., Akoğlu, A. M., Meghraoui, M., & Reilinger, R. (2012). Onset of aseismic creep on major strike-slip faults. Geology, 40(12), 1115–1118. https://doi.org/10.1130/G33522.1

[8] Calais, E., Freed, A., Mattioli, G., Amelung, F., Jónsson, S., Jansma, P., Hong, S.H., Dixon, T., Prépetit, C. and Momplaisir, R., 2010. Transpressional rupture of an unmapped fault during the 2010 Haiti earthquake. Nature Geoscience, 3(11), pp.794-799. https://www.nature.com/articles/ngeo992

[9] Calais, E., Symithe, S., Monfret, T., Delouis, B., Lomax, A., Courboulex, F., Ampuero, J.P., Lara, P.E., Bletery, Q., Chèze, J. and Peix, F., 2022. Citizen seismology helps decipher the 2021 Haiti earthquake. *Science*, *376*(6590), pp.283-287. https://www.science.org/doi/10.1126/science.abn1045

[10] Cao, N., Lee, H., & Jung, H. C. (2016). A Phase-Decomposition-Based PSInSAR Processing Method. IEEE Transactions on Geoscience and Remote Sensing, 54(2), 1074–1090. https://doi.org/10.1109/TGRS.2015.2473818

[11] Cao, Y., Jónsson, S., & Li, Z. (2021). Advanced InSAR Tropospheric Corrections From Global Atmospheric Models that Incorporate Spatial Stochastic Properties of the Troposphere. Journal of Geophysical Research: Solid Earth, 126(5), e2020JB020952. https://doi.org/https://doi.org/10.1029/2020JB020952

[12] Chen, C. W., & Zebker, H. A. (2001). Two-dimensional phase unwrapping with use of statistical models for cost functions in nonlinear optimization. Journal of the Optical Society of America A, 18(2), 338–351. https://doi.org/10.1364/JOSAA.18.000338

[13] Chen, C. W., & Zebker, H. A. (2002). Phase unwrapping for large SAR interferograms: statistical segmentation and generalized network models. IEEE Transactions on Geoscience and Remote Sensing, 40(8), 1709–1719. https://doi.org/10.1109/TGRS.2002.802453

[14] Copley, A. (2014). Postseismic afterslip 30 years after the 1978 Tabas-e-Golshan (Iran) earthquake: observations and implications for the geological evolution of thrust belts. *Geophysical Journal International*, 197, 665-679. https://doi.org/10.1093/gji/ggu023

[15] Copley, A., Hollingsworth, J. and Bergman, E., 2012. Constraints on fault and lithosphere rheology from the coseismic slip and postseismic afterslip of the 2006 Mw7. 0 Mozambique earthquake. Journal of Geophysical Research: Solid Earth, 117(B3). https://rdcu.be/dyKl4

[16] DesRoches R, Comerio M, Eberhard M, Mooney W, Rix GJ., (2011). Overview of the 2010 Haiti Earthquake Earthquake Spectra, Volume 27, Issue 1, suppl1, https://doi.org/10.1193/1.3630129

[17] Delorme, A., & Makeig, S. (2004). EEGLAB: an open source toolbox for analysis of single-trial EEG dynamics including independent component analysis. *Journal of Neuroscience Methods*, 134(1), 9-21. https://pubmed.ncbi.nlm.nih.gov/15102499/

[18] Diao, F., Wang, R., Xiong, X., & Liu, C. (2021). Overlapped Postseismic Deformation Caused by Afterslip and Viscoelastic Relaxation Following the 2015 Mw 7.8 Gorkha (Nepal) Earthquake. *Journal of Geophysical Research: Solid Earth*, 126. https://doi.org/10.1029/2020JB020378

[19] Douilly, R., et al. (2013). Crustal structure and fault geometry of the 2010 Haiti earthquake from temporary seismometer deployments. Journal of Geophysical Research: Solid Earth, 118(10), 5582-5599. https://doi.org/10.1785/0120120303

[20] Dutta, R., and Maurer, J., (2024). Mapping Deformation Processes Using Insar Ps+Ds Timeseries Estimation in Northern California, U.S. Available at SSRN: https://ssrn.com/abstract=4779349 or http://dx.doi.org/10.2139/ssrn.4779349.

[21] Ebmeier, S. K. (2016). Application of independent component analysis to multitemporal InSAR data with volcanic case studies. *Journal of Geophysical Research: Solid Earth*, *121*(12), 8970–8986. https://doi.org/https://doi.org/10.1002/2016JB013765

[22] Even, M., & Schulz, K. (2018). InSAR Deformation Analysis with Distributed Scatterers: A Review Complemented by New Advances. Remote Sensing, 10(5). https://doi.org/10.3390/rs10050744

[23] Ferretti, A., et al. (2001). Permanent scatterers in SAR interferometry. https://ieeexplore.ieee.org/document/898661

[24] Fattahi, H., Agram, P.S., Tymofyeyeva, E. and Bekaert, D.P., 2019. FRInGE; Full-Resolution InSAR timeseries using Generalized Eigenvectors. AGUFM, 2019, pp.G11B-0514. https://ui.adsabs.harvard.edu/abs/2019AGUFM.G11B0514F

[25] Ferretti, A., Prati, C., & Rocca, F. (2001). Permanent scatterers in SAR interferometry. IEEE Transactions on Geoscience and Remote Sensing.

https://doi.org/10.1109/36.898661
[26] Ferretti, A., Prati, C., & Rocca, F. (2000). Nonlinear subsidence rate estimation using permanent scatterers in differential SAR interferometry. IEEE Transactions on Geoscience and Remote Sensing, 38(5), 2202–2212. https://doi.org/10.1109/36.868878
[27] Ferretti, A., Fumagalli, A., Novali, F., Prati, C., Rocca, F., & Rucci, A. (2011). A new algorithm for processing interferometric data-stacks: SqueeSAR. IEEE Transactions on Geoscience and Remote Sensing. https://doi.org/10.1109/TGRS.2011.2124465
[28] Flores, C. H., ten Brink, U. S., & Bakun, W. H. (2012). Accounts of damage from historical earthquakes in the northeastern Caribbean to aid in the determination of their location and intensity magnitudes. In Open-File Report. https://doi.org/10.3133/ofr20111133
[29] Fukuda, J., & Johnson, K. (2021). Bayesian Inversion for a Stress-Driven Model of Afterslip and Viscoelastic Relaxation: Method and Application to Postseismic Deformation Following the 2011 MW 9.0 Tohoku-Oki Earthquake. *Journal of Geophysical Research: Solid Earth*, 126. https://doi.org/10.1029/2020JB021620
[30] Gaddes, M. E., Hooper, A., Bagnardi, M., Inman, H., & Albino, F. (2018). Blind Signal Separation Methods for InSAR: The Potential to Automatically Detect and Monitor Signals of Volcanic Deformation. *Journal of Geophysical Research: Solid Earth*, *123*(11), 10,210-226,251. https://doi.org/https://doi.org/10.1029/2018JB016210
[31] Gualandi, A., & Liu, Z. (2021). Variational Bayesian Independent Component Analysis for InSAR Displacement Time-Series With Application to Central California, USA. *Journal of Geophysical Research: Solid Earth*, *126*(4), e2020JB020845. https://doi.org/https://doi.org/10.1029/2020JB020845
[32] Hanssen, R. F. (2001). Radar interferometry: data interpretation and error analysis. https://link.springer.com/book/10.1007/0-306-47633-9
[33] Hayes, G. P., et al. (2010). Complex rupture during the 2010 Haiti earthquake. Nature Geoscience, 3(11), 800-805. https://www.nature.com/articles/ngeo977
[34] Hough, S. E., Martin, S. S., Symithe, S. J., & Briggs, R. (2022). Rupture Scenarios for the 3 June 1770 Haiti Earthquake. Bulletin of the Seismological Society of America, 113(1), 157–185. https://doi.org/10.1785/0120220108
[35] Hong, S., & Liu, M. (2021). Postseismic Deformation and Afterslip Evolution of the 2015 Gorkha Earthquake Constrained by InSAR and GPS Observations. *Journal of Geophysical Research: Solid Earth*, 126. https://doi.org/10.1029/2020JB020230
[36] Hooper, A., Segall, P., & Zebker, H. (2007). Persistent scatterer interferometric synthetic aperture radar for crustal deformation analysis, with application to Volcán Alcedo, Galápagos. Journal of Geophysical Research: Solid Earth, 112(B7). https://doi.org/https://doi.org/10.1029/2006JB004763
[37] Hooper, A., Zebker, H., Segall, P., & Kampes, B. (2004). A new method for measuring deformation on volcanoes and other natural terrains using InSAR persistent scatterers. Geophysical Research Letters, 31(23). https://doi.org/https://doi.org/10.1029/2004GL021737
[38] Hu, Z., Mallorquí, J.J. and Fan, H., 2018. Atmospheric artifacts correction with a covariance-weighted linear model over mountainous regions. IEEE Transactions on Geoscience and Remote Sensing, 56(12), pp.6995-7008. https://ieeexplore.ieee.org/document/8412159
[39] Hyvärinen, A., & Oja, E. (1997). A fast fixed-point algorithm for independent component analysis. *Neural Computation*, 9(7), 1483-1492. https://ieeexplore.ieee.org/document/6797075
[40] Hyvärinen, A., Karhunen, J., & Oja, E. (2001). *Independent Component Analysis*. John Wiley & Sons. https://onlinelibrary.wiley.com/doi/book/10.1002/0471221317
[41] Hyvärinen, A. (2011). Testing the ICA mixing matrix based on inter-subject or inter-session consistency. *NeuroImage*, *58*(1), 122–136. https://doi.org/10.1016/j.neuroimage.2011.05.086
[42] Hyvärinen, A., & Ramkumar, P. (2013). Testing Independent Component Patterns by Inter-Subject or Inter-Session Consistency. *Frontiers in Human Neuroscience*, *7*. https://doi.org/10.3389/fnhum.2013.00094
[43] Jiang, J. and Lohman, R.B., 2021. Coherence-guided InSAR deformation analysis in the presence of ongoing land surface changes in the Imperial Valley, California. *Remote Sensing of Environment*, *253*, p.112160. https://doi.org/10.1016/j.rse.2020.112160
[44] Jolivet, R., Agram, P. S., Lin, N. Y., Simons, M., Doin, M.-P., Peltzer, G., & Li, Z. (2014). Improving InSAR geodesy using Global Atmospheric Models. Journal of Geophysical Research: Solid Earth, 119(3), 2324–2341. https://doi.org/10.1002/2013JB010588
[45] Johnson, K. M., Wallace, L. M., Maurer, J., Hamling, I., Williams, C., Rollins, C., Gerstenberger, M., & Van Dissen, R. (2024). Inverting Geodetic Strain Rates for Slip Deficit Rate in Complex Deforming Zones: An Application to the New Zealand Plate Boundary. Journal of Geophysical Research: Solid Earth, 129(3), e2023JB027565. https://doi.org/https://doi.org/10.1029/2023JB027565
[46] Kirui, P. K., Riedel, B., & Gerke, M. (2022). Multi-temporal InSAR tropospheric delay modelling using Tikhonov regularization for Sentinel-1 C-band data. ISPRS Open Journal of Photogrammetry and Remote Sensing, 6, 100020. https://doi.org/https://doi.org/10.1016/j.ophoto.2022.100020
[47] Kumar, P. V. V., Dutta, G., Ratnam, M., Krishna, E., Bapiraju, B., Rao, B., & Mohammad, S. (2016). Impact of cyclone Nilam on tropical lower atmospheric dynamics. Advances in Atmospheric Sciences, 33, 955-968. https://doi.org/10.1029/2011JB008580
[48] Lange, D., Bedford, J., Moreno, M., Tilmann, F., Báez, J., Bevis, M., Krüger, F. (2014). Comparison of postseismic afterslip models with aftershock seismicity for three subduction-zone earthquakes: Nias 2005, Maule 2010 and Tohoku 2011. *Geophysical Journal International*, 199, 784-799. https://doi.org/10.1093/gji/ggu292
[49] Liu, N., Spiva, N., Dwyer, J.R., Rassoul, H.K., Free, D. and Cummer, S.A., 2015. Upward electrical discharges observed above Tropical Depression Dorian. Nature Communications, 6(1), p.5995. https://www.nature.com/articles/ncomms6995
[50] Mann, P., et al. (2002). Oblique collision in the northeastern Caribbean from GPS measurements and geological observations. Tectonics, 21(6), 1057. https://doi.org/10.1029/2001TC001304
[51] Martin, S. S., & Hough, S. E. (2022). The 8 April 1860 Jour de Pâques Earthquake Sequence in Southern Haiti. Bulletin of the Seismological Society of America, 112(5), 2468–2486. https://doi.org/10.1785/0120220016
[52] Maurer, J., Dutta, R., Vernon, A., & Vajedian, S. (2022). Complex Rupture and Triggered Aseismic Creep During the 14 August 2021 Haiti Earthquake From Satellite Geodesy. *Geophysical Research Letters*, 49(11), e98573. https://doi.org/10.1029/2022GL098573
[53] Maubant, L., Pathier, E., Daout, S., Radiguet, M., Doin, M.P., Kazachkina, E., Kostoglodov, V., Cotte, N. and Walpersdorf, A., 2020. Independent component analysis and parametric approach for source separation in InSAR time series at regional scale: application to the 2017–2018 Slow Slip Event in Guerrero (Mexico). *Journal of Geophysical Research: Solid Earth*, *125*(3), p.e2019JB018187. https://doi.org/10.1029/2019JB018187
[54] Mirzaee, S., Amelung, F., & Fattahi, H. (2023). Non-linear phase linking using joined distributed and persistent scatterers. Computers & Geosciences, 171, 105291. https://doi.org/https://doi.org/10.1016/j.cageo.2022.105291
[55] Murray, K.D., Bekaert, D.P. and Lohman, R.B., 2019. Tropospheric corrections for InSAR: Statistical assessments and applications to the Central United States and Mexico. *Remote Sensing of Environment*, *232*, p.111326. https://doi.org/10.1016/j.rse.2019.111326
[56] Peng, M., Motagh, M., Lu, Z., Xia, Z., Guo, Z., Zhao, C., & Liu, Q. (2024). Characterization and prediction of InSAR-derived ground motion with ICA-assisted LSTM model. *Remote Sensing of Environment*, *301*, 113923. https://doi.org/https://doi.org/10.1016/j.rse.2023.113923
[57] Pollitz, F. F., Evans, E. L., Field, E. H., Hatem, A. E., Hearn, E. H., Johnson, K., Murray, J. R., Powers, P. M., Shen, Z., Wespestad, C., & Zeng, Y. (2022). Western U.S. Deformation Models for the 2023 Update to the U.S. National Seismic Hazard Model. Seismological Research Letters, 93(6), 3068–3086. https://doi.org/10.1785/0220220143
[58] Prentice, C. S., et al. (2010). Seismic hazard of the Enriquillo–Plantain Garden fault in Haiti inferred from palaeoseismology. Nature Geoscience, 3(11), 789-793. https://www.nature.com/articles/ngeo991
[59] Raimbault, B., Jolivet, R., Calais, E., Symithe, S., Fukushima, Y. and Dubernet, P., 2023. Rupture geometry and slip distribution of the Mw 7.2 Nippes earthquake, Haiti, from space geodetic data. Geochemistry, Geophysics, Geosystems, 24(4), p.e2022GC010752. https://doi.org/10.1029/2022GC010752
[60] Rouet-Leduc, B., Jolivet, R., Dalaison, M., Johnson, P. A., & Hulbert, C.

(2021). Autonomous extraction of millimeter-scale deformation in InSAR time series using deep learning. Nature Communications, 12(1), 6480. https://doi.org/10.1038/s41467-021-26254-3

[61] Sandwell, D. T., et al. (2011). GMTSAR: An InSAR Processing System Based on Generic Mapping Tools. https://escholarship.org/uc/item/8zq2c02m

[62] Shamshiri, R., Motagh, M., Nahavandchi, H., Haghshenas Haghighi, M., & Hoseini, M. (2020). Improving tropospheric corrections on large-scale Sentinel-1 interferograms using a machine learning approach for integration with GNSS-derived zenith total delay (ZTD). Remote Sensing of Environment, 239, 111608. https://doi.org/https://doi.org/10.1016/j.rse.2019.111608

[63] Shanker, P., & Zebker, H. (2007). Persistent scatterer selection using maximum likelihood estimation. Geophysical Research Letters, 34(22). https://doi.org/https://doi.org/10.1029/2007GL030806

[64] Shen, Z.K. and Bird, P., 2022. Neokinema deformation model for the 2023 update to the US National Seismic Hazard Model. Seismological Society of America, 93(6), pp.3037-3052. http://scec.ess.ucla.edu/~zshen/publ/srl22shen.pdf

[65] Siddique, M. A., Strozzi, T., Hajnsek, I., & Frey, O. (2019). A Case Study on the Correction of Atmospheric Phases for SAR Tomography in Mountainous Regions. IEEE Transactions on Geoscience and Remote Sensing, 57, 416-431. https://ieeexplore.ieee.org/document/8450633

[66] Tymofyeyeva, E. and Fialko, Y., 2015. Mitigation of atmospheric phase delays in InSAR data, with application to the eastern California shear zone. *Journal of Geophysical Research: Solid Earth*, *120*(8), pp.5952-5963. https://doi.org/10.1002/2015JB011886

[67] Tymofyeyeva, E., Agram, P.S., Fattahi, H. and Bekaert, D.P., 2019. Transient creep on the Concord Fault, Eastern Bay Area, revealed by InSAR time series. AGUFM, 2019, pp.T13D-0304.

[68] U.S. Geological Survey. (2021). Landslides Triggered by the August 14, 2021, Magnitude 7.2 Nippes, Haiti, Earthquake. U.S. Geological Survey Open-File Report 2021-1112. https://doi.org/10.3133/ofr20211112.

[69] Yu, C., Li, Z., Penna, N. T., & Crippa, P. (2018). Generic atmospheric correction model for Interferometric Synthetic Aperture Radar observations. *Journal of Geophysical Research: Solid Earth, 123*(10), 9202-9222. https://doi.org/10.1029/2018JB016079

[70] Yu, C., Li, Z., & Penna, N. T. (2018). Interferometric synthetic aperture radar atmospheric correction using a GPS-based iterative tropospheric decomposition model. *Remote Sensing of Environment, 204*, 109-121. https://doi.org/10.1016/j.rse.2017.10.038

[71] Yu, C., Penna, N. T., & Li, Z. (2017). Generation of real-time mode high-resolution water vapor fields from GPS observations. *Journal of Geophysical Research: Atmospheres, 122*(3), 2008-2025. https://doi.org/10.1002/2016JD025753

[72] Zoe Yin, H., Xu, X., Haase, J. S., Douilly, R., Sandwell, D. T., & Mercier de Lepinay, B. (2022). Surface Deformation Surrounding the 2021 Mw 7.2 Haiti Earthquake Illuminated by InSAR Observations. Bulletin of the Seismological Society of America, 113(1), 41–57. https://doi.org/10.1785/0120220109

[73] Zebker, H., Shankar, P., & Hooper, A. (2007). InSAR Remote Sensing Over Decorrelating Terrains: Persistent Scattering Methods. 2007 IEEE Radar Conference, 717–722. https://doi.org/10.1109/RADAR.2007.374307

[74] Zebker, H. (2021). Accuracy of a Model-Free Algorithm for Temporal InSAR Tropospheric Correction. In *Remote Sensing* (Vol. 13, Issue 3). https://doi.org/10.3390/rs13030409